Halide perovskites for direct conversion megavoltage x-ray detectors

Soumya Kundu, Jericho O'Connell, Alexander Hart, Devon Richtsmeier, Magdalena Bazalova-Carter & Makhsud I. Saidaminov

2022

Original citation:

Kundu, S., O'Connell, J., Hart, A., Richtsmeier, D., Bazalova-Carter, M., & Saidaminov, M. I. (2022). Halide perovskites for direct conversion megavoltage x-ray detectors. *Advanced Electronic Materials, 8*(12). https://doi.org/10.1002/aelm.202200640

ADVANCED ELECTRONIC MATERIALS
www.advelectronicmat.de

Halide Perovskites for Direct Conversion Megavoltage X-Ray Detectors

*Soumya Kundu, Jericho O'Connell, Alexander Hart, Devon Richtsmeier, Magdalena Bazalova-Carter, and Makhsud I. Saidaminov**

Megavoltage (MV) X-ray detectors used in cancer treatment either suffer from low sensitivity (scintillators) or prohibitively high cost (direct conversion). Here solution-processed direct-conversion MV X-ray detectors are demonstrated based on halide perovskites. The authors' prototype devices show a sensitivity of ≈0.7 μC Gy_{air}^{-1} cm^{-2}, high photon-to-carrier conversion efficiency of 42 500%, and a signal-to-noise ratio of ≈1750 to 6 MV X-ray beam of a medical linear accelerator. The detector shows a contrast of over −1.5% per cm of solid water, comparable to state-of-art commercial gadolinium oxysulfide (GOS) MV X-ray scintillators. This work demonstrates the first prototype of low-cost and efficient direct-conversion MV X-ray detectors.

1. Introduction

Depending on their energy, X-ray interacts differently with the matter. Lower-energy kilovoltage (kV) X-rays are sensitive to differences in tissue composition and are therefore used in medical imaging. On the other hand, higher-energy megavoltage (MV) X-rays are characterized by deeper tissue penetration and lower sensitivity to tissue composition and are therefore used in cancer treatment. Photon sensors determine the accuracy and efficiency of both X-ray medical applications. Such sensors are able to directly convert X-ray photons to electrical signals (called direct converters) or indirectly through visible photons (scintillators). Direct converters generally offer simpler configurations and higher resolution than indirect converters.

$Cd_{1-x}Zn_xTe$-based direct conversion X-ray detectors have been commercialized for kV X-ray imaging. However, their use in MV X-ray sensors, which require orders of magnitude thicker materials, is prohibitively costly. Therefore, commercial MV detectors are based on scintillators, mainly gadolinium oxysulfide (GOS). Unfortunately, GOS absorbs its own scintillation photons: this property limits the thickness of GOS detectors to <0.3 mm, which in turn deteriorates the detector's resolution and sensitivity.[1] As a result, MV X-ray machines are usually equipped with a complementary kV X-ray imaging system for patient alignment. This increases the complexity and the cost of conventional X-ray treatment machines. Partly due to the high cost of such treatment machines, in 2020 alone, more than 70% of 10.35 million new registered cases of cancer in low and middle-income countries had no access to proper treatment for their disease.[2] The development of low-cost radiotherapy treatment machines, which combine real-time dosimetry and direct-conversion imaging during treatment, is imperative for improving cancer outcomes. In addition, developing direct MV sensors would lead to high atomic number artifact reduction, MV imaging for patient setup, and real-time dosimetry during treatments.

Here we report a direct conversion MV X-ray detector based on solution-processed methylammonium lead bromide ($MAPbBr_3$) perovskite crystals. Due to its high density (3.8 g cm^{-3}) and high atomic number (Z_{eff} = 67.2), $MAPbBr_3$ offers excellent photon absorption in the MV range. Our prototype device shows a high photon-to-carrier conversion efficiency of ≈42 500%, a high signal-to-noise ratio of ≈1750 and the contrast of over −1.5% per cm of solid water to 6 MV X-ray being comparable to state-of-art commercial GOS detectors.

2. Experimental Section

2.1. Materials

Methylamine solution (40 wt% in H_2O), HBr (48% in H_2O), and $PbBr_2$ (≥98%) were purchased from Sigma-Aldrich. Gold (99.999%) was purchased from Angstrom Engineering. Gallium (99.99%) was purchased from Amazon. DMF was purchased from Fisher Scientific. All chemicals were used without further purification.

MABr was synthesized by following standard procedure. 86.4 mL of methylamine solution (40 wt% in H_2O) was added

S. Kundu, M. I. Saidaminov
Department of Chemistry
University of Victoria
Victoria, British Columbia V8P 5C2, Canada
E-mail: msaidaminov@uvic.ca
J. O'Connell, A. Hart, D. Richtsmeier, M. Bazalova-Carter
Department of Physics and Astronomy
University of Victoria
Victoria, British Columbia V8P 5C2, Canada
The ORCID identification number(s) for the author(s) of this article can be found under https://doi.org/10.1002/aelm.202200640.

DOI: 10.1002/aelm.202200640

to a 4 L round bottom flask and was put in an ice bath. 1000 mL of 95% ethanol was added to the flask. Then a 118.8 mL of HBr solution was added with a dripping funnel slowly with continuous stirring over an hour. After complete addition, the mixture was stirred for another 2 h to maximize the yield. Then the solvent was evaporated. The solid was dissolved in a minimum amount of boiling ethanol. After complete dissolution, the solution was left undisturbed overnight for crystallization. The white MABr solid crystals were filtered out and washed with diethyl ether and dried under vacuum for more than 24 h.

2.2. Crystal Synthesis

The growth solution was prepared by dissolving 1.4 M $PbBr_2$ and 1.43 M MABr in DMF overnight with continuous stirring. Then the solution was left undisturbed for 12 h. The solution was filtered to a 15 cm crystallizing dish by 0.45 µm PVDF syringe filters before crystallization. The hot plate temperature was set to 36 °C. To grow a high quality single crystal, a small single crystal (<1 mm) was added as seed. The dish was covered with plastic wrap and a few holes were made with a needle to enable slow evaporation of DMF. The temperature of the hot plate was slowly increased from 36 to 40 °C with a rate of 1 °C h^{-1}. The crystal seed started to grow. Then the temperature of the hot plate was increased to 45 °C, with 2 °C day^{-1} rate. The temperature was kept at 45 °C for 3 days. To control the solvent evaporation and decrease the growth rate the temperature of the hot plate was decreased 0.5 °C day^{-1} to 39 °C. Finally, a large size crystal of 6.6 cm × 6.4 cm × 1.7 cm crystal was harvested which is the largest $MAPbBr_3$ single crystal ever reported.

2.3. X-Ray Detector Fabrication

The X-ray detectors were fabricated by depositing gold and gallium on two flat sides of a perovskite single crystal.

2.4. Characterization

pXRD measurements were done on a PANalytical Empyrean system using a Cu (K_α, 1.5406 Å) source. The $MAPbBr_3$ powder was produced by grinding a single crystal into fine powder in a mortar.

SCLC devices were fabricated by depositing 100 mm thick gold in the opposite sides of the single crystals by thermal evaporation with a rate of 0.4 kÅ s^{-1}. The dark *I*–*V* curve was recorded using a Keithley 2450. The thicknesses of the $MAPbBr_3$ single crystals were measured by a digital vernier caliper.

The trap density (n_{traps}) was calculated from the trap-filled region using the following equation:[3]

$$n_{traps} = \frac{2V_{TFL}\varepsilon_r\varepsilon_0}{eL^2} \quad (1)$$

where V_{TFL} is the trap-filled limit voltage, L is the thickness of the crystal, ε_r is the relative dielectric constant ($\varepsilon_r = 25.5$),[4] ε_0 is the vacuum permittivity, and e is the electron charge. The trap density was calculated based on six devices.

The carrier mobility for the $MAPbBr_3$ single crystal was further calculated for the trap-free region (blue lines) according to the Mott–Gurney law:[5]

$$\mu = \frac{8J_{SCLC}L^3}{9\varepsilon\varepsilon_0 V_{SCLC}^2} \quad (2)$$

where J_{SCLC} is the current density. As expected, the $MAPbBr_3$ single crystal exhibited a quite high hole carrier mobility of $107 \pm 42\ cm^2\ V^{-1}\ s^{-1}$.

2.5. Monte Carlo Simulations

Energy deposition efficiency was used as a measure of the relative quantum efficiency of the perovskite crystals as compared to the current TrueBeam aS1200 detector's GOS scintillator. Energy deposition efficiency was used as a proxy for the readout of the two detectors, respectively, as the method of readout for the two detectors are indirect and direct, respectively: The GOS scintillator was readout through scintillation photons incident on the amorphous silicon readout while the perovskite crystal was readout by the charge accumulated through the generation of electron–hole pairs in the crystal. However, both readout signals would be proportional to the energy deposited in the crystals. This assumption was also conservative as it gave benefit to the GOS detector which had internal attenuation of a portion of its scintillation photons before readout, a feature that will not be taken into account by measuring energy deposition efficiency. Thus, since the measurement was conservative in this way, it was proposed as a valid method of demonstrating potential quantum efficiency benefit of perovskite in this application.

The energy deposition efficiency at an energy e, η_e, was defined in terms of ratio of the incident energy $E_{e,i}$ on the detector to the energy absorbed in the crystal $E_{e,abs}$ from a mono-energetic pencil beam at energy e impinging on the detector at an angle of 90° relative to the detector

$$\eta_e = \frac{E_{e,i}}{E_{e,abs}} \quad (3)$$

Simulations of energy deposition efficiency were performed in Topas with 1 000 000 initial particles per energy per crystal thickness.[6] The mono-energetic pencil beam energies used were 10–90 keV in 10 keV increments, 100–900 keV in 100 keV increments, and 1, 2, 4, and 6 MeV a greater emphasis of energies in the low kV range was used to help resolve photo-electric behavior near the k-edges of crystal elements. Simulations were run on a Linux desktop computer on 8 4.0 GHz Intel Skylake cores with a compute time of 37 min. A global particle range cutoff of 0.001 mm was used to remain much smaller than the minimum crystal thickness of 0.29 mm.

Both detectors were designed after the Varian aS1200 EPID which features a 2.5 mm carbon fiber cover. It should be noted that the GOS scintillator on the aS1200 detector was not a pure GOS crystal but rather a composite of terbium doped GOS granules suspended in a polyurethane elastomer, in this case

with a fill factor of 60%, resulting in an overall composite density of 4.59 g cm^{-3}. This particular detector material specification was used as it is the standard imager on Varian linacs and was typically used as a baseline for detector performance.[7,8] The perovskite had a density 3.8 g cm^{-3} while both detectors featured thin layers of meltmount glue as an adhesive and low density foam for shock absorption as well as 5 cm of water as backing on the beam to provide realistic backscatter. Complete densities and dimensions of the detector can be found in O'Connell and Bazalova-Carter.[9]

Fractional photon absorption for a 6 MV beam was also calculated to demonstrate the efficiency of photon absorption for the GOS and perovskite crystals, respectively, for a beam commonly used for MV imaging. The 6 MV beam was derived from the manufacturer-provided TrueBeam phasespace file. Calculations of fractional absorption were calculated using the Fastcat simulation python package, which calculates fractional photon absorption (ε) from summing the fractional fluence (ψ_e) multiplied by the energy deposition (η_e) at discrete energies

$$\varepsilon = \sum \psi_e \eta_e \tag{4}$$

Values for energy deposition efficiency for both detectors were measured in the way described previously in this section.

2.6. Detector Performance

Megavoltage X-ray measurements were conducted with a Varian TrueBeam linear accelerator (Palo Alto, USA) actively used for radiotherapy treatments. All measurements were performed with a peak beam energy of 6 mega electron volts (6 MV) and dose rate was varied from 3.33 to 16.6 mGy s^{-1}. The linear accelerator was calibrated according to the TG-51 protocol to deliver 10 mGy s^{-1} at 100 cm source to axis distance, at a depth of 1.5 cm in water.

The response of the $MAPbBr_3$ device to 6 MV X-rays was measured using a PTW UNIDOS E electrometer (Freiburg, Germany) in current mode at 2 frames per second. Sensitivity was assessed by measuring three 15 s irradiations at dose rates of 3.3, 6.6, 10, 13.3, and 16.6 mGy s^{-1}. Ion chamber measurements confirmed that the X-ray output was linear over this dose rate range. Image contrast was assessed by measuring current with varying thicknesses of solid water (Sun Nuclear, Melbourne, USA) attenuating the X-ray beam at a dose rate of 10 mGy s^{-1}. The performance of the single pixel prototype $MAPbBr_3$ device was compared against contrast measurements obtained with the GOS MV imaging panel on board the TrueBeam. The GOS contrast measurements were obtained under similar conditions to the perovskite crystal, with the detector panel positioned 100 cm from the source and irradiated with 15 MU at each solid water thickness. The integrated signal from both the perovskite crystal and a single pixel from the GOS panel were normalized to the reading obtained with 2 cm of solid water attenuating the beam.

Relative contrast was then calculated for solid water thicknesses up to 15 cm, according to:

$$\%\text{Contrast} = (I_{2\text{cm}} - I_x)/I_{2\text{cm}} \tag{5}$$

where $I_{2\,\text{cm}}$ is the integrated signal acquired with 2 cm of solid water and I_x is the integrated signal with x cm of solid water attenuating the X-rays. Pixel corrections or smoothing was not applied to either detector.

A current versus voltage (I–V) curve was measured for the $MAPbBr_3$ device using a PTW UNIDOS E electrometer (Freiburg, Germany) electrometer while irradiated with 6 MV X-rays at dose rates of 10 mGy s^{-1}.

2.7. Calculation of the Sensitivity

The sensitivity of the detector was evaluated based on the ON/OFF photocurrent response under a certain applied bias for a 6 MV X-ray beam. The X-ray dose rate was varied by changing the X-ray tube current. The photocurrent showed a linear relationship with the X-ray dose rate, as plotted in Figure S5, Supporting Information. The sensitivity of the device at a 50 V applied bias was extracted by calculating the slope of the linear fit form of Figure S5, Supporting Information.

X-ray sensitivity (S) of the detectors was calculated by the following equation

$$s = \frac{\Delta I}{DA} \tag{6}$$

where ΔI is the photocurrent ($\Delta I = I_{\text{light}} - I_{\text{dark}}$), D is the dose rate of incident X-ray radiation, and A is the area of the detector.

2.8. Photon-to-Carrier Conversion Efficiency

To calculate photon-to-carrier conversion, the input photon flux of 6 MV X-rays generated from Varian TrueBeam linear accelerator (Palo Alto, USA) was simulated. It was assumed that the X-rays beam was hitting the detector at a solid angle. The detector was placed at a distance of 10 cm from the source. The electric field was applied in an area, of 8.5 × 8 mm^2. The X-ray photon flux, F, onto the $MAPbBr_3$ detector was calculated to be 3.4×10^{11} photons Gy^{-1} based on Monte-Carlo simulation.

From the value of the photocurrent $\Delta I = I_{\text{light}} - I_{\text{dark}}$ produced by a detector with a penetration depth of 13 mm and active length of 8 mm. The MV X-ray photon-to-charge carrier generation efficiency, η (charge carriers per absorbed photon), was estimated as:

$$\begin{aligned}\eta &= \frac{\text{Output charges}}{\text{Absorbed photons}} \\ &= \frac{\text{Current}(\text{A/s}) \times \text{Number of electrons/A}}{\text{Input photons flux}(\text{photons}/G\gamma) \times \text{Dose rate}\left(\frac{G\gamma}{\text{s}}\right) \times \text{Fraction of photons absorbed}}\end{aligned} \tag{7}$$

Figure S4, Supporting Information, depicts the structure of the MV X-ray detector. According to the authors' Monte-Carlo simulation, 30% of the photon flux was absorbed by the 13 mm thick area of the single crystal. The remaining 70% of the photon flux was hitting the active area (Figure S4,

Supporting Information). Considering the diffusion length of the carriers (≈10 µm) were much lower than the length of the crystal (≈mm), the electrodes did not collect the carriers generated in the 13 mm length. The carriers generated within the 8 mm active area were only being collected, which was 20% of entering flux, or (20% of 70%) 14% of the initial flux. Therefore, based on the above equation, the conversion efficiency for 6 MV X-rays with a dose rate of 10 mGy s^{-1} under 400 V applied bias was ≈42 500% for 6 MV X-rays. Note that external quantum efficiency (EQE) for MeV was expected to be much lower due to limited absorption of MeV photons.

2.9. Calculation of Signal-to-Noise Ratio

The signal-to-noise ratio (SNR) was calculated using equation:

$$\mathrm{SNR} = \frac{I_{\mathrm{signal}}}{I_{\mathrm{noise}}} \tag{8}$$

the signal current (I_{signal}) was calculated by subtracting the average photocurrent (I_{photo}) by the average dark current (I_{dark}). The noise current (I_{noise}) was the standard deviation of the photocurrent.

The operational stability of the detector was measured with ≈1 Hz 30 kVp X-ray pulses.

3. Results and Discussion

Solution-processed metal halide perovskites have recently emerged as a family of unique semiconductors for kV X-ray detectors.[10] Due to their elemental constitution of heavy atoms such as lead, metal halide perovskites have a high X-ray attenuation coefficient and high density.[10a,c,11]

We first simulated the energy deposition efficiency (EDE) on both perovskite and GOS with Monte Carlo simulation to assess their ability to absorb MV X-rays (**Figure 1**a,b). Both materials showed a sharp rise in EDE starting at 20 keV and peaking at 100 keV with maximum energy deposition efficiencies of 0.69 and 0.64 for 15 mm GOS and perovskite detectors, respectively. The maximum EDE was sustained over a larger range of values for the perovskite than the GOS detector. The EDE then dropped off slowly at higher energies in the MV range for both detectors.

The EDE difference plot between the two materials shows three regions separated by the K-edge of lead and gadolinium (Figure 1c). There is an ≈30% increase in the EDE of Perovskite relative to GOS between 10 and 55 keV for thin detectors. After 55 keV the increased photoelectric absorption of gadolinium causes it to be a better photoelectric absorber leading to a 7% advantage in EDE. After 88 keV, the k-edge of lead in perovskite again leads to a higher EDE with an ≈5% advantage over GOS. The GOS tends to have higher EDE at higher energies due to its greater density, which makes it a better Compton absorber.[12] For thicker detectors, the regions are shifted to higher energies due to the absorption scatter in the detector, which makes photoelectric interactions a source of backscatter, reducing the EDE. Note that our analysis overestimates GOS' EDE as it allows orders of magnitude thicker GOS than its practical limit (<0.3 mm) discussed above.

Overall, for MV detection, the region of interest in Figure 1c is the area between 200–1000 keV where perovskite has a ≈20% higher EDE than GOS since this is the energy where much of the fluence of a 6 MV photon beam is produced. For a beam commonly used for MV imaging, 6 MV beam derived from the manufacturer-provided TrueBeam phase-space file, perovskite again shows an advantage over GOS (Figure 1d).

3.1. Single Crystal Growth and Characterization

Motivated by the Monte-Carlo simulations, we aimed to grow large $MAPbBr_3$ perovskite single crystals. We first started with slow evaporation of the precursor solution at low temperature as the slow growth rate can lead to better crystal quality with fewer defects. However, room-temperature evaporation from DMF, which has a boiling point of 153 °C, takes months to grow large single crystals. Inverse temperature crystallization (ITC) addresses the slow growth rate, but leads to many nucleation centers (Figure S1, Supporting Information).[13]

We therefore combined ITC with solvent-evaporation technique, that is, left the crystallization setup open during ITC. We started with a 1.4 M $MAPbBr_3$ solution in DMF, placed a mm-sized seed crystal, and started the crystallization at 40 °C, with a ramp of 2 °C day^{-1} until 55 °C. Although the crystal grew into more than an inch in a few days, it became irregular and opaque due to the high growth rate and oversupply of solute (**Figure 2**a).

This process was further optimized to control the crystallization growth rate. We again started the crystallization at 40 °C with a small seed crystal at a rate of 2 °C day^{-1}, but only until 45 °C. Until this temperature, the crystallization process is dominated by ITC, showing a maximum growth rate (Figure 2a,b). We then kept the temperature constant at 45 °C for 3 days; at this stage, the crystal growth is dominated by solvent evaporation. To suppress additional nucleation and defect densities, we then slowly decreased the temperature to 39 °C at –0.5 °C day^{-1}. We also added an excess of MABr into the growth solution to suppress secondary nucleation. This method of alternating ITC and solvent-evaporation modes of crystallization led to 76% product yield, twice as high as typical ITC. The crystal size reached a dimension of 6.6 cm × 6.4 cm × 1.7 cm, weighing ≈261 g (Figure 2b), one of the largest perovskite single crystals reported to date. Based on the cost of precursors (MABr, $PbBr_2$, and DMF), the estimated price of the $MAPbBr_3$ single crystals is in the order of approximately US$ 1.0 per cm^3.[14]

X-ray diffraction (XRD) of the ground single crystal shows a single phase that corresponds to the cubic $MAPbBr_3$ (Figure 2c). XRD of an intact single crystal shows only a family of <100> peaks indicating the single-crystal nature of our material.

We then studied the electronic properties of the crystals. Hole-only devices were made by depositing gold on both sides of the single crystals. The dark current-voltage (*I*–*V*) characteristics of $MAPbBr_3$ SCs (Figure 2d) exhibit three regions: an ohmic region at a low bias ($<V_{\mathrm{TFL}}$), a trap-filling region where the current abruptly increases, and a Child region at a higher

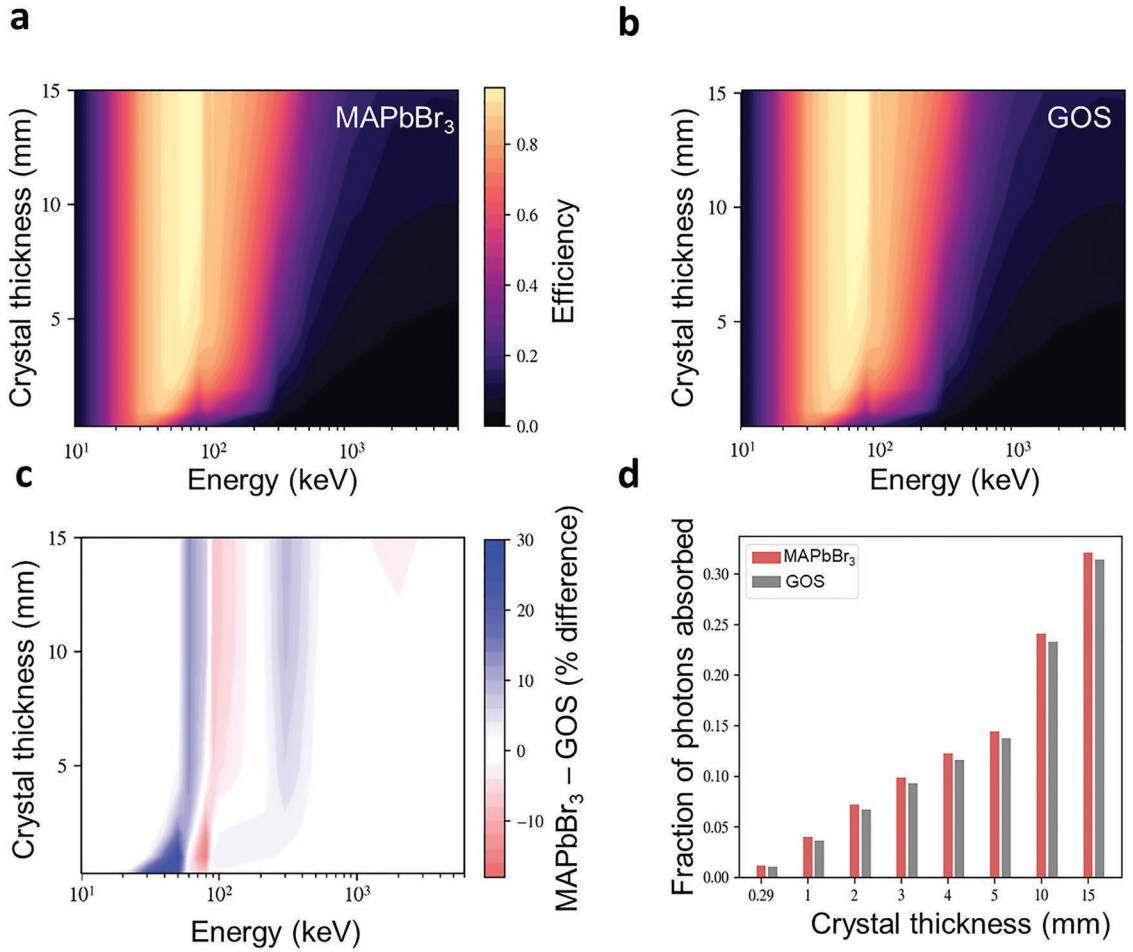

Figure 1. Monte-Carlo simulations of detection efficiency. a,b) Monte-Carlo calculations of energy deposition efficiency of mono-energetic pencil beams impinging on $MAPbBr_3$ and GOS at energies between 10 keV and 6 MeV for different detector thicknesses. c) The contour plot of the difference between the EDE of $MAPbBr_3$ and GOS with variable thickness. d) Monte-Carlo simulation of fractional photon absorption as a function of crystal thickness in $MAPbBr_3$ and GOS crystals for a 6 MV TrueBeam photon beam.

bias. The carrier mobilities and the trap densities (n_{traps}) were estimated to be $107 \pm 42\,cm^2\,V^{-1}s^{-1}$ and $(7.69 \pm 3.1) \times 10^9$ cm^{-3} for 6 $MAPbBr_3$ crystals, which are comparable to the literature values (Figure 2d, **Table 1**). The high carrier mobility and ultralow trap density indicate excellent crystal quality.

Carrier mobility-to-lifetime ($\mu\tau$) product is another parameter to evaluate the carrier transport capability of the crystals. The $\mu\tau$ product was extracted by fitting current–voltage characteristic at 30 kVp X-ray beam by modified Hecht equation[18] and was found to be 7.4×10^{-3} cm^2 V^{-1} (Figure S2, Supporting Information). This is among one of the highest values reported in literature.[13,5,15–17]

3.2. MV X-Ray Detector Performance

To devise an MV X-ray detector, we chose an asymmetric electrode configuration where one metal, Au, has a lower work function (hole collector) than the other, Ga (electron collector) as displayed in **Figure 3**a. This significantly reduces the dark current of the detector.[19] The dark current of the detector was 0.755 nA cm^{-2} under a large electric field of $667\,V\,cm^{-1}$. In addition, the dark current of the device is very stable with time (Figure S3, Supporting Information).

We exposed our device to 6 MV X-rays produced by the TrueBeam linear accelerator. To maximize the absorption of the high-energy photons, we oriented the crystal in the vertical direction (Figure S4, Supporting Information). The current–voltage (*I–V*) characteristics at dark and under 6 MV X-ray dose of 10 mGy s^{-1} show a clear photocurrent response (Figure 3b).

The response of devices to MV X-rays was also demonstrated by turning the incident 6 MV X-rays ON and OFF, as presented in Figure 3c. We observed a steady increase in the photocurrent signal with increased X-ray beam energy that showed excellent linearity with dose rates from 3.33 to 16.6 mGy s^{-1} (Figure S5, Supporting Information). The sensitivity of the detector, estimated from the slope of Figure S5, Supporting Information, was found to be $\approx 0.7\,\mu C\,Gy_{air}^{-1}\,cm^{-2}$.

We then estimated the photon-to-charge conversion efficiency of $MAPbBr_3$ detector (see Supporting Information for

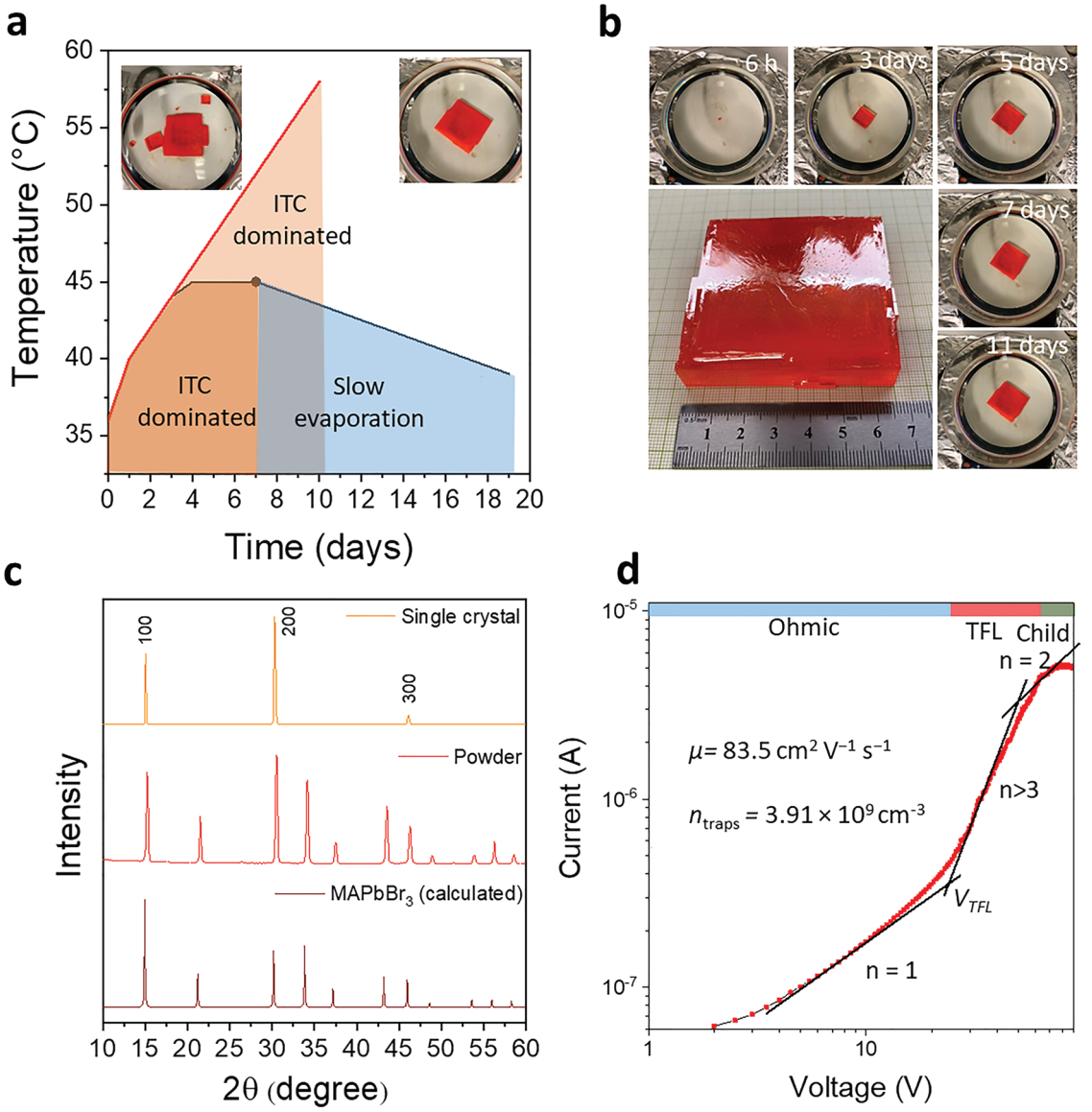

Figure 2. $MAPbBr_3$ single crystal growth. a) Temperature profile of the two crystal growth methods. Insets: photographs of crystals grown by ITC-dominated method and modified method. b) Photographs of $MAPbBr_3$ crystallization with modified ITC method. c) XRD of ground and intact $MAPbBr_3$ crystal. d) Current–voltage characteristics of the single crystal. Inset: statistics of the calculated trap densities for multiple $MAPbBr_3$ single crystals grown using modified ITC method.

Table 1. Performance metrics of $MAPbBr_3$ SCs with different growth methods.

Methods	Temperature [°C]	Dimension (volume) [mm^3]	Time	Trap density [cm^{-3}]	References
AVC	RT	≈7 × 7 × 3	7 days	5.8×10^9	[15]
STCAD	36	50 × 50 × 21	15 days	$\approx10^{10}$	[16]
ITC	>80	≈7 × 7 × 3	3 h	3.0×10^{10}	[13]
LTGC	60	47 × 41 × 14	20 days	6.7×10^9	[5]
LDSC	RT	≈10 × 10 × 4	>5 days	4.4×10^9	[17]
ITC/slow evaporation	40–45	67 × 64 × 17	18 days	3.91×10^9	This work

details). Conversion efficiency increases with the decrease in dose rate (Figure 3d) and with the increase in electrical field (Figure 3e) due to efficient carrier collection. The detector showed a conversion efficiency of up to ≈42 500% per absorbed 6 MV X-ray photon.

We also estimated the signal-to-noise ratio (SNR) of our detector by varying the MV X-ray dose rate at a constant applied bias (Figure 3f). With the increase in the X-ray dose rate, we observed a significant increase in SNR, and it reached up to 917 for 83.3 mGy s^{-1} at 50 V applied bias. To study the dependence of SNR with applied voltage, we varied the applied bias at 10 mGy s^{-1} X-ray dose rate. With an increase in the applied voltage, we observed a significant increase in SNR, reaching as high as ≈1750 under 350 V (Figure 3g).

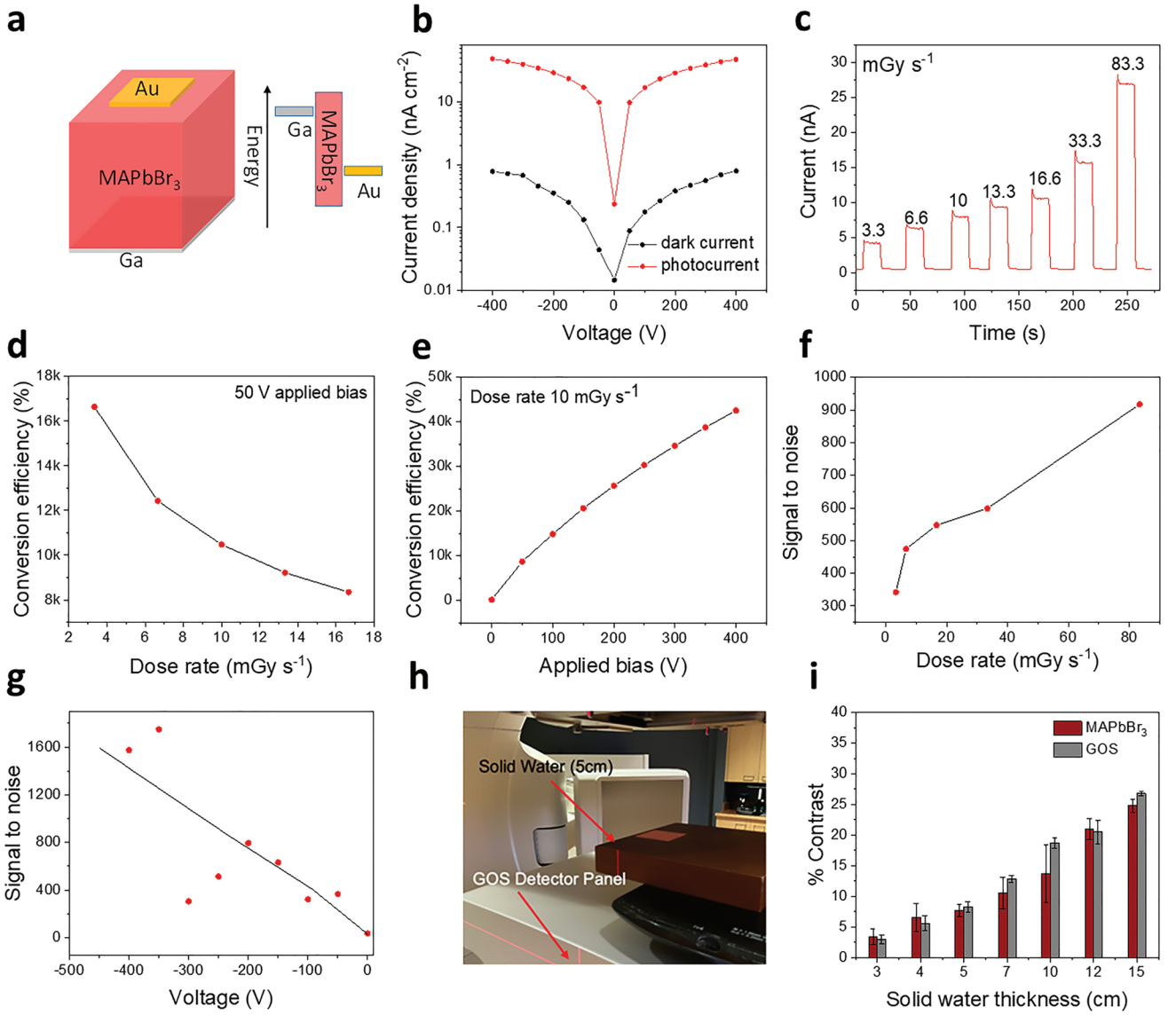

Figure 3. a) Schematic illustration of the structure of Au/$MAPbBr_3$/Ga MV detector, and its corresponding energy level diagram. b) *I–V* characteristics of Au/$MAPbBr_3$/Ga MV detector under dark and 6 MV 10 mGy s^{-1} X-rays illumination. c) ON/OFF photocurrent response of the detector under various dose rates at 6 MV X-rays at 50 V applied bias. X-ray attenuation with crystal thickness. d) Dose rate dependence photon-to-carrier conversion efficiency of Au/$MAPbBr_3$/Ga detector at 50 V applied voltage. e) Change of photon-to-carrier conversion efficiency with applied bias at 10 mGy s^{-1} dose rate. f) SNR of the detector as a function of X-ray dose rate at 50 V applied bias. g) SNR of the detector as a function of different bias voltage at 10 mGy s^{-1} dose rate. h) Photography of contrast measurement setup on a TrueBeam. i) Contrast with respect to thicknesses of solid water.

Contrast is a crucial figure of merit for MV imaging. We evaluated the contrast of our single-pixel $MAPbBr_3$ detectors with 6 MV X-rays beam using a setup shown in Figure 3h. We chose solid water blocks (density of 1.032 g cm^{-3}) for the measurement to mimic the human tissue density (1.0346 g cm^{-3}).[20] Output photocurrent was measured with varying thicknesses of solid water blocks (Figure 3i; Figure S6, Supporting Information). Due to the high penetration depth of high-energy photons of MV X-rays, MV imagers often suffer from poor contrast. However, our detector exhibits a clear contrast showing a significant drop in the photocurrent signal between the different layers of solid water blocks (Figure S6, Supporting Information). We then compared the contrast performance of our detector to the state-of-the-art GOS panel on board the TrueBeam, which showed a similar performance to our $MAPbBr_3$ detector (Figure 3i).

We measured ON/OFF response of our detector with 30 kVp X-ray beam pulses to determine the baseline drift during speedy charging and discharging (**Figure 4**). We found stable response to 100 pulses with no drift of dark current indicating of stable operational response of our detector.

In conclusion, we have demonstrated a novel crystal growth method to grow large and high-quality halide perovskite crystals that is required to build high performance MV X-ray detectors. The detectors made from such crystals have proven to

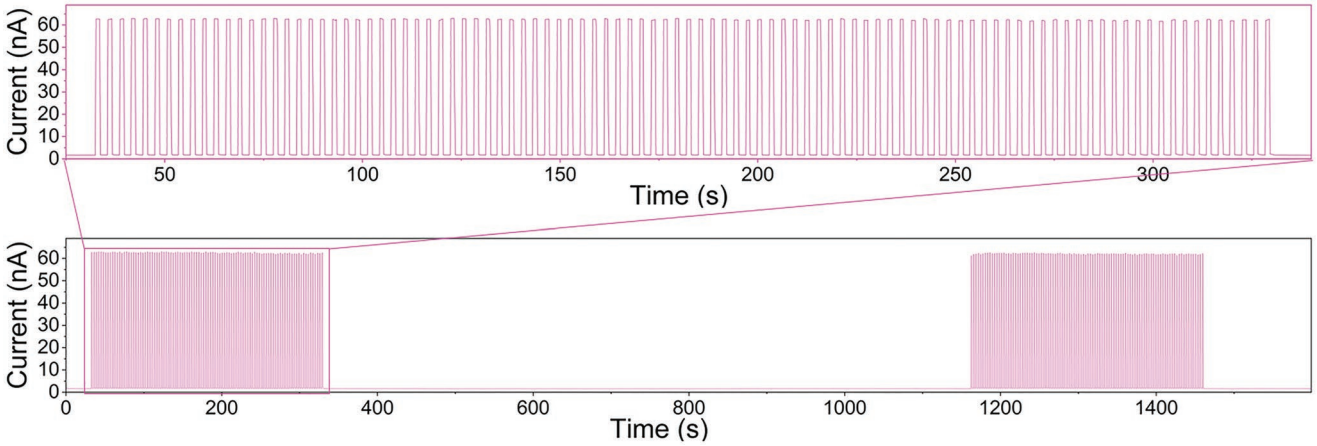

Figure 4. ON/OFF response of the device to 30 kVp X-ray fast pulses.

have excellent photon-to-carrier conversion efficiency, signal-to-noise ratio, and contrast to MV X-rays under direct conversion mode, and are already comparable to those of state-of-art GOS detectors. This work demonstrates first of its kind low-cost direct-conversion MV X-ray detector.

Supporting Information

Supporting Information is available from the Wiley Online Library or from the author.

Acknowledgements

This work was supported by New Frontiers in Research Fund—Exploration and University of Victoria Collaborative Health Grant. The authors thank BC Cancer (Provincial Health Services Authority in British Columbia, Canada) for providing the testing facility. The authors thank Jon Eby for developing an X-ray shutter system which enabled high frequency measurements.

Conflict of Interest

The authors declare no conflict of interest.

Author Contributions

S.K., J.O., and A.H. contributed equally to this work. The crystallization approach, device fabrication, samples preparation for measurements, XRD, and SCLC experiments were done by S.K. The measurements on the devices with X-ray was done by A.H. and D.R. Monto-Carlo simulation was performed by J.O. The manuscript was co-written by S.K., J.O., A.H., and M.I.S. and commented by all authors. The work was supervised by M.I.S. and M.B.-C.

Data Availability Statement

The data that support the findings of this study are available from the corresponding author upon reasonable request.

Keywords

crystallization, inch long single crystals, lead halide perovskites, megavoltage X-ray detectors

Received: June 16, 2022
Revised: August 25, 2022
Published online: October 17, 2022

[1] J. Star-Lack, M. Sun, A. Meyer, D. Morf, D. Constantin, R. Fahrig, E. Abel, *Med. Phys.* **2014**, *41*, 031916.
[2] H. Sung, J. Ferlay, R. L. Siegel, M. Laversanne, I. Soerjomataram, A. Jemal, F. Bray, *Cancer J. Clin.* **2021**, *71*, 209.
[3] R. H. Bube, *J. Appl. Phys.* **1962**, *33*, 1733.
[4] A. Poglitsch, D. Weber, *J. Chem. Phys.* **1987**, *87*, 6373.
[5] Y. Liu, Y. Zhang, Z. Yang, J. Feng, Z. Xu, Q. Li, M. Hu, H. Ye, X. Zhang, M. Liu, K. Zhao, S. Liu, *Mater. Today* **2019**, *22*, 67.
[6] J. Perl, J. Shin, J. Schumann, B. Faddegon, H. Paganetti, *Med. Phys.* **2012**, *39*, 6818.
[7] J. Star-Lack, D. Shedlock, D. Swahn, D. Humber, A. Wang, H. Hirsh, G. Zentai, D. Sawkey, I. Kruger, M. Sun, E. Abel, G. Virshup, M. Shin, R. Fahrig, *Med. Phys.* **2015**, *42*, 5084.
[8] M. Shi, M. Myronakis, Y. H. Hu, D. Morf, J. Rottmann, R. Berbeco, *Phys. Med. Bio.* **2018**, *63*, 165013.
[9] J. O'Connell, M. Bazalova-Carter, *Med. Phys.* **2021**, *48*, 4448.
[10] a) H. Wei, J. Huang, *Nat. Commun.* **2019**, *10*, 1066; b) H. Wu, Y. Ge, G. Niu, J. Tang, *Matter* **2021**, *4*, 144; c) X. Xu, W. Qian, S. Xiao, J. Wang, S. Zheng, S. Yang, *EcoMat* **2020**, *2*, e12064; d) Z. Li, F. Zhou, H. Yao, Z. Ci, Z. Yang, Z. Jin, *Mater. Today* **2021**, *48*, 155; e) A. Datta, Z. Zhong, S. Motakef, *Sci. Rep.* **2020**, *10*, 20097; f) H. Li, J. Song, W. Pan, D. Xu, W.-a. Zhu, H. Wei, B. Yang, *Adv. Mater.* **2020**, *32*, 2003790; g) Y. Zhou, J. Chen, O. M. Bakr, O. F. Mohammed, *ACS Energy Lett.* **2021**, *6*, 739; h) S. Das, S. Gholipour, M. Saliba, *Energy Environ. Mater.* **2019**, *2*, 146; i) S. Yakunin, M. Sytnyk, D. Kriegner, S. Shrestha, M. Richter, G. J. Matt, H. Azimi, C. J. Brabec, J. Stangl, M. V. Kovalenko, W. Heiss, *Nat. Photonics* **2015**, *9*, 444; j) X. Gong, O. Voznyy, A. Jain, W. Liu, R. Sabatini, Z. Piontkowski, G. Walters, G. Bappi, S. Nokhrin, O. Bushuyev, M. Yuan, R. Comin, D. McCamant, S. O. Kelley, E. H. Sargent, *Nat. Mater.* **2018**, *17*, 550; k) A. Mei, X. Li, L. Liu, Z. Ku, T. Liu, Y. Rong, M. Xu, M. Hu, J. Chen, Y. Yang, M. Grätzel, H. Han, *Science* **2014**, *345*, 295; l) N. K. Tailor, S. Kar, P. Mishra, A. These, C. Kupfer, H. Hu,

M. Awais, M. Saidaminov, M. I. Dar, C. Brabec, S. Satapathi, *ACS Mater. Lett.* **2021**, *3*, 1025; m) R. Lin, J. Xu, M. Wei, Y. Wang, Z. Qin, Z. Liu, J. Wu, K. Xiao, B. Chen, S. M. Park, G. Chen, H. R. Atapattu, K. R. Graham, J. Xu, J. Zhu, L. Li, C. Zhang, E. H. Sargent, H. Tan, *Nature* **2022**, *603*, 73; n) M. K. Gangishetty, R. W. J. Scott, T. L. Kelly, *Nanoscale* **2016**, *8*, 6300; o) S. Kundu, D. Richtsmeier, A. Hart, V. Yeddu, Z. Song, G. Niu, D. Thrithamarassery Gangadharan, E. Dennis, J. Tang, O. Voznyy, M. Bazalova-Carter, M. I. Saidaminov, *Adv. Opt. Mater.* **2022**, *10*, 2200516.

[11] a) X. Zheng, W. Zhao, P. Wang, H. Tan, M. I. Saidaminov, S. Tie, L. Chen, Y. Peng, J. Long, W.-H. Zhang, *J. Energy Chem.* **2020**, *49*, 299; b) H. Tsai, F. Liu, S. Shrestha, K. Fernando, S. Tretiak, B. Scott, D. T. Vo, J. Strzalka, W. Nie, *Sci. Adv.* **2020**, *6*, eaay0815; c) C. Ma, F. Chen, X. Song, M. Chen, L. Gao, P. Wang, J. Wen, Z. Yang, Y. Tang, K. Zhao, S. Liu, *Adv. Funct. Mater.* **2021**, *31*, 2100691.

[12] a) P. Sukumar, S. Padmanaban, P. Jeevanandam, S. A. Syam Kumar, V. Nagarajan, *Rep. Pract. Oncol. Radiother.* **2011**, *16*, 248; b) C. Penner, C. Hoehr, S. O'Keeffe, P. Woulfe, C. Duzenli, *IEEE Sens. J.* **2018**, *18*, 1513.

[13] M. I. Saidaminov, A. L. Abdelhady, B. Murali, E. Alarousu, V. M. Burlakov, W. Peng, I. Dursun, L. Wang, Y. He, G. Maculan, A. Goriely, T. Wu, O. F. Mohammed, O. M. Bakr, *Nat. Commun.* **2015**, *6*, 7586.

[14] S. Yakunin, D. N. Dirin, Y. Shynkarenko, V. Morad, I. Cherniukh, O. Nazarenko, D. Kreil, T. Nauser, M. V. Kovalenko, *Nat. Photonics* **2016**, *10*, 585.

[15] D. Shi, V. Adinolfi, R. Comin, M. Yuan, E. Alarousu, A. Buin, Y. Chen, S. Hoogland, A. Rothenberger, K. Katsiev, Y. Losovyj, X. Zhang, P. A. Dowben, O. F. Mohammed, E. H. Sargent, O. M. Bakr, *Science* **2015**, *347*, 519.

[16] L. Zhang, Y. Liu, X. Ye, Q. Han, C. Ge, S. Cui, Q. Guo, X. Zheng, Z. Zhai, X. Tao, *Cryst. Growth Des.* **2018**, *18*, 6652.

[17] F. Yao, J. Peng, R. Li, W. Li, P. Gui, B. Li, C. Liu, C. Tao, Q. Lin, G. Fang, *Nat. Commun.* **2020**, *11*, 1194.

[18] R. Zhuang, X. Wang, W. Ma, Y. Wu, X. Chen, L. Tang, H. Zhu, J. Liu, L. Wu, W. Zhou, X. Liu, Y. Yang, *Nat. Photonics* **2019**, *13*, 602.

[19] Y. He, L. Matei, H. J. Jung, K. M. McCall, M. Chen, C. C. Stoumpos, Z. Liu, J. A. Peters, D. Y. Chung, B. W. Wessels, M. R. Wasielewski, V. P. Dravid, A. Burger, M. G. Kanatzidis, *Nat. Commun.* **2018**, *9*, 1609.

[20] T. W. Barber, J. A. Brockway, L. S. Higgins, *Acta Neurol. Scand.* **1970**, *46*, 85.